Diffusion Coefficient of Cyclic GMP in Salamander Rod Outer Segments Estimated with Two Fluorescent Probes

Andrew Olson* and Edward N. Pugh, Jr.‡

*Institute of Neurological Sciences, University of Pennsylvania, and the ‡Department of Psychology and Institute of Neurological Sciences, University of Pennsylvania, Philadelphia, Pennsylvania 19104 USA

ABSTRACT Experiments have demonstrated that single photoisomerizations in amphibian and primate rods can cause the suppression of 3–5% of the dark circulating current at the response peak (Baylor, D. A., T. D. Lamb, and K. W. Yau. 1979. *J. Physiol. (Lond.).* 288:613–634; Baylor, D. A., B. J. Nunn, and J. L. Schnapf. 1984. *J. Physiol. (Lond.).* 357:575–607.). These results indicate that the change in [cGMP] effected by a single isomerization must spread longitudinally over at least the corresponding fractional length of the outer segment. The effective longitudinal diffusion coefficient, D_x, of cGMP is thus an important determinant of rod sensitivity.

We report here measurements of the effective longitudinal diffusion coefficients, D_x, of two fluorescently labeled molecules: 5/6-carboxyfluorescein and 8-(fluoresceinyl)thioguanosine 3′,5′-cyclic monophosphate, introduced into detached outer segments via whole-cell patch electrodes. For these compounds, the average time for equilibration of the entire outer segment with the patch pipette was ~6 min. Fluorescence images of rods were analyzed with a one-dimensional diffusion model that included limitations on transfer between the electrode and outer segment and the effects of intracellular binding of the dyes. The analyses yielded estimates of D_x of 1.9 and 1.0 $\mu m^2 \cdot s^{-1}$ for the two dyes. It is shown that these results place an upper limit on D_x for cGMP of 11 $\mu m^2 \cdot s^{-1}$. The actual value of D_x for cGMP in the rod will depend on the degree of intracellular binding of cGMP. Estimates of the effective buffering power for cGMP in the rod at rest range from two to six (Lamb and Pugh, 1992; Cote and Brunnock, 1993). When combined with these estimates, our results predict that for cGMP itself, D_x falls within the range of 1.4–5.5 $\mu m^2 \cdot s^{-1}$.

INTRODUCTION

The "cyclic GMP cascade" is now well established as the biochemical process underlying phototransduction in vertebrate photoreceptors (reviewed in Stryer (1986); Pugh and Lamb (1993)). The process comprises five major steps of activation: 1) a photoisomerized visual pigment molecule becomes an active enzyme, R*; 2) the active enzyme R* catalyzes the exchange of GTP for GDP on an outer segment G-protein ("transducin"), producing an active moiety, T*—the α-subunit of transducin with GTP bound; 3) T* in turn binds to a phosphodiesterase, relieving an inhibition imposed by its γ-subunit, producing an active enzyme, PDE*; 4) PDE* catalyzes the hydrolysis of cytoplasmic cGMP, causing the concentration of free cGMP to decline in the photoreceptor outer segment; 5) cGMP-activated cation channels in the plasma membrane close as mass action produces a decline in channels with adequate cGMP bound to them. The closing of the cGMP channels causes a decrease in the standing "dark," or circulating, current, hyperpolarizing the photoreceptor. Associated with each activation step of the cascade there are one or more inactivation (or restoration) processes, which are required for the termination of the photoresponse; many aspects of restoration and inactivation remain poorly understood (see e.g., Pugh and Lamb (1990, 1993)).

Before the cGMP cascade theory was proposed in its presently accepted form, it was recognized that phototransduction in rods requires an internal messenger to communicate excitation between the discs and the plasma membrane, and also that the excitation must spread longitudinally in the rod outer segment. The latter conclusion was based upon the findings that the light-sensitive current is uniformly distributed over the length of the outer segment (Hagins et al., 1970; Baylor et al., 1979) and that a single photoisomerization causes the suppression of 3–5% of this current at response peak (Baylor et al., 1979, 1984). In addition to demonstrating the longitudinal spread of excitation, experiments also showed that the spread was limited in extent (Hagins et al., 1970; Lamb et al., 1981). Reinterpreted in terms of the cGMP cascade theory, the evidence just cited shows that the spatial profile of the decrement in cGMP in response to a single photoisomerization must be determined in part by the longitudinal diffusion of cGMP in the outer segment. Thus, any quantitatively complete theory of phototransduction must include an account of cGMP diffusion, i.e., of the effect of cGMP diffusion on the kinetics and amplification of the photoresponse.

The goal of this investigation was to estimate the effective longitudinal diffusion coefficient of cGMP. Previous estimates of the longitudinal diffusion coefficient have been obtained in studies in which the spread of photoactivation (Lamb et al., 1981) or of cGMP-activated current (Cameron and Pugh, 1990) was measured. In this study the movement of two cGMP "analogs," 5/6-carboxyfluorescein (CF) and 8-(fluoresceinyl)thioguanosine 3′,5′-cyclic monophosphate (fl-cGMP) (see Fig. 1), introduced into outer segments from whole-cell pipettes was measured. From the application of

Received for publication 10 February 1993 and in final form 1 June 1993.

Address reprint requests to Dr. Edward N. Pugh, Jr., Department of Psychology, University of Pennsylvania, 3815 Walnut Street, Philadelphia, PA 19104-6196.

0006-3495/93/08/1335/18 $2.00

diffusion theory to the spread of fluorescence, we obtained estimates of the effective longitudinal diffusion coefficients of these analogs, and from these estimates, we infer bounds on the effective longitudinal diffusion coefficient of cGMP.

METHODS

Cell preparation

Larval tiger salamanders (*Ambystoma tigrinum*, Lowrance Waterdog Farms, Tulsa, OK; or Charles D. Sullivan, Nashville, TN) were decapitated and pithed under dim red illumination. The eyes were removed, and the retinas were dissected from each eye under infrared illumination. For some experiments, tissue was obtained from an eye stored overnight at 4°C in a moist, sealed container. Whole-cell currents recorded from such cells have been shown to be indistinguishable from those of freshly obtained cells (Perri, 1991). Cells were dissociated by chopping a piece of retina using a small piece of razor blade held with forceps, in a dish coated with 3–5 mm of Sylgard elastomer (Dow Corning, Midland, MI) and filled with ~2 ml of salamander Ringer's solution (contains, in millimolar: 2.5 KCl, 110 NaCl, 1.0 $CaCl_2$, 2.0 $MgCl_2$, 1.0 NaH_2PO_4, 5.0 $NaHCO_3$, 0.05 Na_2EGTA, 10 4-(2-hydroxyethyl)-1-piperazineethanesulfonic acid (HEPES); pH 7.35–7.40). Bovine serum albumin (BSA, 0.2% w/v) also was added to the solution in the chopping dish.

For several experiments, an enzymatic dissociation procedure was used. 66 μl of papain suspension (816 units/ml, Worthington Biochemical, Freehold, NJ) was added to 2.0 ml of activating solution (contains, in millimolar: 5.4 KCl, 0.25 Na_2HPO_4, 10.8 EDTA, 20 HEPES, 5 cysteine (added at time of use); pH 7.0) and activated at 25°C for 30 min. The activated papain solution was then diluted 1:2 with salamander Ringer's solution in a chopping dish. Retinal hemisections were added and incubated at 25°C for 30–40 min with intermittent agitation. The enzyme solution was then removed from the dish, and the tissue was rinsed with several changes of salamander Ringer's +0.2% BSA. After enzyme treatment, dissociated rods and rod outer segments were easily obtained either by chopping (as above) or by repeated trituration of small retinal pieces with a P20 Pipetman (5-μl setting).

A small volume (1–2 μl) of cell suspension from the chopping dish was pipetted into the recording chamber and then mounted on the stage of an inverted microscope (Zeiss IM-35) for video and electrical recording.

Electrical recording

Whole-cell electrodes were pulled from Corning 0100 glass (Garner Glass, Claremont, CA). Tip resistances ranged from 4 to 15 MΩ when filled with internal solution (contains, in millimolar: 100 potassium aspartate, 10 NaCl, 1.0 $NaHCO_3$, 3.5 $MgCl_2$, 1.0 $MgSO_4$, 0.1 K_2EGTA, 10 HEPES; pH 7.35–7.40), plus varying amounts of either CF (0.5–2.2 mM) or (fl-cGMP, 0.5 mM). Both compounds were obtained from Molecular Probes, Eugene, OR; see Fig. 1.

The electrode was brought near to the cell under infrared illumination and was visualized on a television monitor using an image intensifier coupled to a CCD camera (models C2400-97 and C2400-77H; Photonic Microscopy, Oak Brook, IL). A few of the early CF experiments were performed using a video camera equipped with an extended infrared silicon vidicon (Dage-MTI, Michigan City, IN). A 2-mV command pulse was superimposed on the holding potential, V_h,[1] the tip resistance of the electrode was measured, and

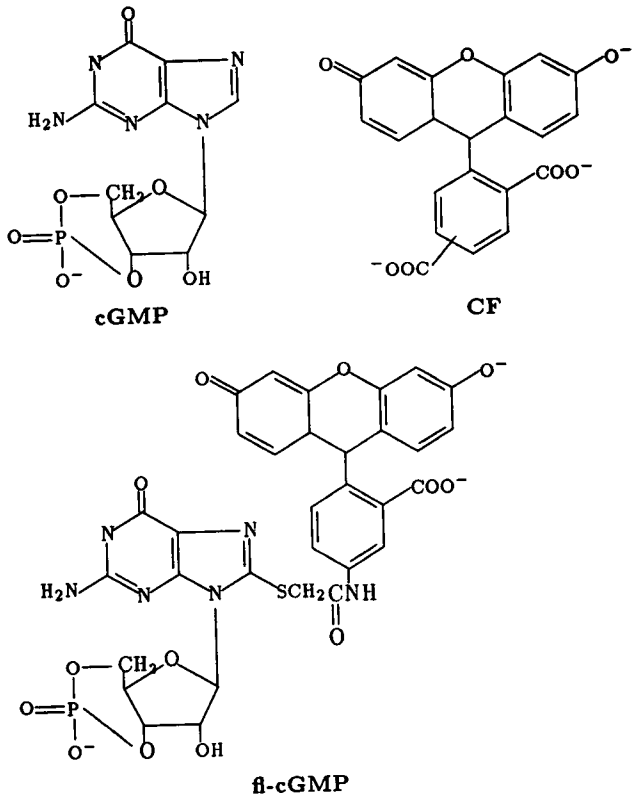

FIGURE 1 Structure of cGMP and fluorescent analogs. Chemical structures of cyclic GMP (M_r = 345), 5/6-carboxyfluorescein (M_r = 376) and fluorescein-cyclic GMP (M_r = 764).

the series resistance compensation of the whole-cell recording amplifier (model 8900; Dagan Corporation, Minneapolis, MN) was set accordingly. The electrode was maneuvered into contact with the desired region of the cell, and a tight seal was formed with gentle suction. At this point in the experiment, the microscope was carefully refocused for the visible fluorescence emission; the necessary offset from the correct focus for infrared illumination had been determined previously and was read from the focusing knob vernier. The holding potential and series resistance compensation circuits were also activated at this time. Whole-cell access was obtained by further gentle suction, or in some cases by spontaneous rupture of the membrane patch.

Fluorescence recording

The inverted microscope was equipped with an epifluorescence system, modified as follows. The excitation source was a 100-W mercury vapor arc lamp (model HBO 100 W/2; Osram, Berlin, Germany) powered by a constant-current source (model 990015; LEP Ltd., Scarsdale, NY). The lamp housing was enclosed in a light-tight box and ventilated with forced air. This enclosure was mounted to the microscope via an electronically controlled shutter (Uniblitz, Vincent Associates, Rochester, NY) attached to a standard Zeiss mount. An infrared-blocking filter was placed in the light path to prevent heating of the tissue. For most of the CF experiments, the standard Zeiss fluorescein filter set (BP 450–490 excitation filter, FT 510 dichroic beam splitter, LP 520 barrier filter) was used. For later CF and all fl-cGMP experiments, a new dichroic beam splitter was used (model 505DRLP; Omega Optical, Brattleboro, VT), and the barrier filter was replaced with

[1] Cameron and Pugh (1990), reported a significant gradient of membrane potential along the length of the outer segment when high concentrations of cGMP were infused from a patch pipette. Since infusions of fl-cGMP would be expected to have a similar effect, V_h was set at 0 mV for all fl-cGMP experiments in order to avoid producing an electrophoretic driving force on fl-cGMP. In the case of CF, which does not open the cGMP-gated channel, V_h was not relevant—the electrode seal constitutes the principle resistance to ground, thus no electrophoretic differential along the length of the outer segment is expected.

a Kodak Wratten 21 gelatin filter held between two round cover slips. We found that this arrangement allowed less of the scattered excitation light to pass through to the camera, thus enhancing the signal-to-noise ratio. We confirmed that the optical recording system responded linearly with light and that the intensity of the excitation light was homogeneous over the entire field. CF fluorescence intensity has been shown to be linear with dye concentration over the range used in this study (Chen and Knutson, 1988).

The intensity of the fluorescence excitation beam was measured with a calibrated planar photodiode (PIN 10DF; United Detector Technology, Hawthorne, CA; absolute calibration by the National Research Council, Canada) in photovoltaic mode. Light from the excitation lamp was attenuated with a calibrated neutral density filter and passed through a 10-μm-diameter pinhole (Melles-Griot, Irvine, CA) placed in the sample plane, before reaching the photodiode. The spectral energy distribution of the excitation lamp, bandpass properties of the fluorescence excitation filter, spectral sensitivity of the photodiode, and absorbance spectra of the dyes, are all known, so from this measurement we were able to calculate the effective quantal flux density, Q_{eff}, of the fluorescence excitation lamp for the two dyes. Q_{eff} was found to be 7.8×10^9 quanta$\cdot\mu m^{-2}\cdot s^{-1}$.

The time constant for bleaching, τ_b, of each dye is given by

$$\tau_b = \frac{1}{Q_{eff}\gamma_b\alpha_{\lambda_{max}}}, \quad (1)$$

γ_b is the quantum efficiency for photodestruction and $\alpha_{\lambda_{max}}$ is the extinction coefficient [in μm^2] of the respective dye molecule at the dye λ_{max}.

The quantum efficiency for photodestruction of fluorescein has been reported as 3×10^{-5} (Mathies and Stryer, 1986). Assuming that CF and fl-cGMP have the same quantum efficiency for photodestruction, we found τ_b = 440 s for CF and, for fl-cGMP, τ_b = 360 s.

The cell fluorescence was recorded at regular intervals after whole-cell access by opening the epifluorescence shutter for ~500 ms. Given the bleaching time constants calculated above, the expected fractional bleach during the 500-ms exposure is 0.11% for CF and 0.14% in the case of fl-cGMP. Consistent with this estimate, we observed no measurable decrement in fluorescence during exposure to the excitation lamp of up to several seconds. The video signal was recorded on XBR videotape with a high-fidelity VCR (model VO-9800; Sony Corporation, Tokyo, Japan). The shutter command signal for the excitation source was recorded on one of the audio tracks for synchronization of image acquisitions during subsequent data analysis.

Fluorescence data analysis

Fluorescence images from videotape were processed digitally with an image analysis system (ITI Series 151; Imaging Technology, Waltham, MA) controlled by a PC-AT computer. The recorded shutter command signal was fed to the computer via a Schmitt trigger circuit and was used to initiate frame acquisition by the image processor. Usually, the 16 successive frames of the half-second fluorescence exposure were digitally averaged and saved. A specified region of the cell image then could be scanned, and the background light values subtracted to obtain a fluorescence intensity profile of the region of interest (see Fig. 4). Such profiles were obtained at all the time points recorded for a particular cell. The set of profiles then was analyzed, as described in the Theory section, to obtain the longitudinal diffusion coefficient (D_x) for the dye in question.

We report fluorescence intensity in terms of the eight-bit digitized values stored in the frame buffer of the image analysis system, and refer to these units as the "pixel amplitude" (p.a.). The absolute scale of this unit varies from cell to cell, since it is dependent on the gain settings for the image-intensified CCD camera, which had to be adjusted for each cell to make best use of the limited dynamic range of the image intensifier.

During the course of an experiment, some cells began to approach saturation in fluorescence intensity because of limitations in the dynamic range of the recording system (principally due to the limited range of the image intensifier). To overcome this problem, two images were recorded in quick succession, with the image intensifier gain reduced for the second "snap." The reduced gain insured that the fluorescence intensity remained within the linear range of the system; comparison of the two successive snaps gave us the correction factor for the reduced gain.

THEORY: DIFFUSION MODEL

Longitudinal diffusion model

In the rod outer segment, radial diffusion is expected to be much faster than longitudinal diffusion; that is, relative to the time needed for longitudinal equilibration of a diffusing substance, radial equilibration is rapid (Baylor et al., 1979; Lamb et al., 1981) (see also Fig. 4). Thus, at any point in time, the outer segment is expected to be radially isotropic in concentration of a diffusing substance, and the analysis of longitudinal diffusion is reduced to a problem in one dimension. We now present a brief exposition of the one-dimensional diffusion model used in this paper (a more detailed treatment, including a discussion of the model parameters, is provided in the Appendix).

Initial and boundary conditions

Fig. 2 shows a rod outer segment of length l. The pipette is assumed to act as an infinite point source of concentration, C_∞, located at some arbitrary position, $x = p$, $0 \le p \le l$ (in microns). The following initial and boundary conditions for the concentration of dye in the cell were assumed: 1) prior to whole-cell access there is no dye inside the cell (Eqs. A3 and A4); 2) the ends of the cell are assumed to act as reflective (no-flux) boundaries (Eqs. A5 and A6); 3) after whole-cell access, at the position of the pipette the concentration of dye in the cell rises monotonically to its final, equilibrated concentration as a function of time, $C_\infty\Phi(t)$, where $\Phi(t)$ is a "softened" unit step function; i.e., $\lim_{t\to\infty}\Phi(t) = 1$ (Eqs. A7, A8, and A9).

The three-parameter family of functions $\{\Phi(t)\colon \tau_1; \tau_2; \tau_3\}$ that we selected to represent the time course of equilibration at the pipette position is a rich set of softened step functions that includes the instantaneous step and exponential rise as special cases. While embodying the general constraint that the dye in the cell at the pipette position comes into equilibrium with the dye in the pipette (Eqs. A7 and A8), the

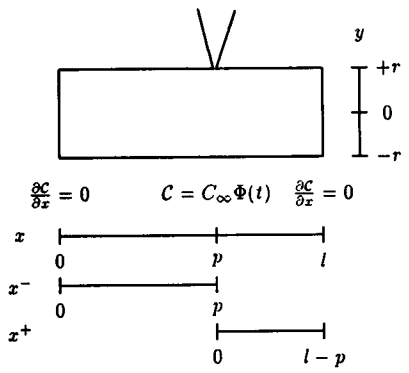

FIGURE 2 Initial and boundary conditions. Illustration of initial and boundary conditions (see text).

family of functions allows for a variety of plausible trajectories of concentration increase. Moreover, $\Phi(t)$ has the advantage of being incorporated readily into an analytical solution for the diffusion equation. The validity of this approach to the problem of equilibration is examined in Results (see Fig. 11).

Diffusion equation

Although photodestruction of the dyes was not found to be significant during the course of an experiment, we were concerned that leakage of dye through the cell membrane may be a significant cause of loss. Therefore, the general equation governing dye diffusion was taken to be

$$\frac{\partial C(x,t)}{\partial t} = D_x \frac{\partial^2 C(x,t)}{\partial x^2} - \nu_L C(x,t). \quad (2)$$

Here, x is position in μm; $C(x, t)$ is the concentration of (free) dye at (x, t) (molar); D_x ($\mu m^2 \cdot s^{-1}$) is the effective longitudinal diffusion coefficient (see Eq. 3); and ν_L (s^{-1}) is the rate constant of dye loss. For a cell initially homogeneous in dye concentration, $1/\nu_L$ gives the time it would take for the concentration to fall $1/e$-fold.

Longitudinal diffusion of a substance in the rod outer segment can be slowed (relative to aqueous diffusion) by 1) the physical hindrance of the discs, 2) cytoplasmic viscosity, and 3) binding of the substance to relatively immobile sites. The model captures these three effects with a single constant, χ (cf. Parameter Ranges). Thus, the effective longitudinal diffusion coefficient, D_x, is defined relative to the aqueous diffusion coefficient, D_{aq}, by:

$$D_x = \chi D_{aq}. \quad (3)$$

The solution to Eq. 2 for the boundary conditions described above is given in Eqs. A10 and A11, which together describe the concentration profile of the *free* dye.

The emitted fluorescence is proportional to the incident light intensity, Q_{eff}, and to the total concentration of dye (both free and bound), with a correction, according to Beer's law, for the possible effect of self-screening by the dye (see discussion of the potential effects of dye binding, under Parameter Ranges). The total emitted fluorescence, $\mathscr{E}$, is thus expected to obey

$$\mathscr{E}(x,t) = \gamma Q_{eff}[1 - 10^{-\epsilon d BC(x,t)}], \quad (4)$$

where γ is the dye's quantum efficiency for fluorescence; ϵ ($M^{-1} \cdot cm^{-1}$) is the molar extinction coefficient at the absorbance maximum for each dye (values: 58,000 $M^{-1} \cdot cm^{-1}$ for CF, 70,000 $M^{-1} \cdot cm^{-1}$ for fl-cGMP); d (cm) is the diameter of the rod outer segment; $B \equiv [\text{dye}]_{total}/[\text{dye}]_{free}$ (see Parameter Ranges).

Finally, $\mathscr{E}$ was convolved with an empirically determined optical linespread function, $\mathscr{L}_\Lambda$, (see Eq. 8 and Fig. 3), and scaled by a factor, S, which relates the quantal units of ϵ to our measured pixel amplitude (p.a.). The predicted fluorescence profile, $\mathscr{F}(x, t)$, is thus given by

$$\mathscr{F}(x,t) = S\mathscr{E} * \mathscr{L}_\Lambda, \quad (5)$$

where $\mathscr{F}(x, t)$ is expressed in units of p.a. (range, 0–255); S (p.a. per quanta$\cdot \mu m^{-2} \cdot s^{-1}$ fluorescence emission) combines several factors related to the optical recording system's collection efficiency (see Parameter Ranges); Λ (μm), is the optical linespread space constant determined for each cell (see Fig. 3); and $*$ signifies convolution.

Fitting procedure

The values of p and l (Eqs. A10–A12) were determined for each cell from the video records. A directed-search program (STEPIT, J. P. Chandler, University of Oklahoma and the Quantum Chemistry Program Exchange, Department of Chemistry, Indiana University, Bloomington, IN), based on the Nelder-Mead simplex algorithm, searched the parameter space to minimize a function of the root-mean-squared (RMS) error between the fluorescence scan data and the fitted data points ($\mathscr{F}(x, t)$, Eq. 5). In order to facilitate comparison between cells and to weight equally the contribution of each fluorescence scan to the error function, the RMS error was expressed as a percentage of the peak fluorescence intensity for each time point; the mean value of these percentage errors was the quantity that the fitting program sought to minimize. Thus, for a cell having measured fluorescence intensities $f(x_j, t_i)$ and computed fluorescence intensities $\mathscr{F}(x_j, t_i)$, with $j = \{0, 1, 2, \ldots, N\}$, and $i = \{0, 1, 2, \ldots, M\}$, the error function, E_{RMS}, would be calculated as

$$E_{RMS} = \frac{100}{M} \sum_{i=0}^{M} \frac{1}{f_{pk}(t_i)} \left\{ \frac{\sum_{j=0}^{N} [f(x_j,t_i) - \mathscr{F}(x_j,t_i)]^2}{N} \right\}^{1/2}, \quad (6)$$

where $f_{pk}(t_i)$ is the measured peak fluorescence intensity (above background) at time t_i, and $\mathscr{F}(x_j, t_i)$ is the computed fluorescence intensity at x_j, t_i (Eq. 5).

Radial distribution of dye

Rapid radial equilibration is a key assumption of the one-dimensional model of diffusion in the outer segment. We examined the validity of this assumption by comparing transverse scans (i.e., scans parallel to the y axis of Fig. 2) with a model of the fluorescence distribution expected for dye radially equilibrated in a volume with circular cross-section. Accordingly, the fluorescence measured from a transverse scan should be directly proportional to the path length, with a small correction for possible self-screening. The expected radial fluorescence distribution, $\mathscr{E}(x, y, t)$, at $x = x_0$ will be given by

$$\mathscr{E}(x_0,y,t) = (1 - y^2/r^2)^{1/2}[1 - 10^{-\epsilon z(y) BC(x,t)}]$$
$$\text{for} \quad -r \le y \le r, \quad (7)$$

where r is the outer segment radius and $z(y)$, the path length (cm), is given by $z(y) = 2(r^2 - y^2)^{1/2}$. We note that Eq. 7 generalizes Eq. 4 (under the assumption of radial isotropy); the latter can be seen to be the special case of Eq. 7 in which $y = 0$. As before, $\mathscr{E}$ must be scaled by S and convolved with the linespread function to give the predicted transverse fluorescence distribution.[2]

RESULTS

Before turning to the longitudinal diffusion measurements, we first present results describing the determination of the optical linespread functions, results that address the assumption of radial isotropy and results from electron micrographs that yield estimates of the tortuosity factor F_A/F_V.

Optical linespread function

An optical linespread function for each cell was determined by the following procedure. First, a scan was made across the most sharply defined edge of the cell (Fig. 3 *A*). For this purpose, we generally chose the proximal end of the outer segment (the former inner-segment/outer-segment boundary). The background light was subtracted, and the edge scan was then normalized by its peak value (Fig. 3 *B*). We then convolved a unit step function with the linespread function, $\mathscr{L}_\Lambda$, defined by

$$\mathscr{L}_\Lambda = \frac{3}{2\Lambda\Gamma(1/3)} \exp(-|\Delta x|^3/\Lambda^3). \quad (8)$$

Here Γ is the gamma function, and $\Delta x = x - x_0$, where x_0 is the position of the line on the x axis. The form of this function was determined empirically, exponents of power 1 or 2 did not provide sufficient steepness to fit the experimental data well. The "space constant," Λ, was varied systematically until the best fit to the normalized edge scan was obtained, as judged by eye (Fig. 3 *c*). The mean "space constant," Λ, (mean ± SEM) for all 16 cells (seven CF, nine fl-cGMP) was 2.0 ± 0.1. If Λ was varied by more than ±5% from the chosen value, the linespread function provided a noticeably poorer fit to the data.

Radial isotropy

Because we expected radial diffusion to be relatively rapid, we did not expect to be able to resolve radial diffusion of dye, given the temporal resolution of our image analysis system (30 ms/frame) and the method of dye introduction. Nonetheless, we examined the fluorescence scans for evidence of radial anisotropy, and we compared the transverse scans with the prediction based upon radial isotropy (Eq. 7). Fig. 4 illustrates how this was done. Longitudinal scans were made at the three locations indicated by dashed boxes in Fig. 4 *A*. When scaled to account for the differences in path length, the traces superimpose almost perfectly, as expected, if radial equilibration is complete (Fig. 4 *B*).

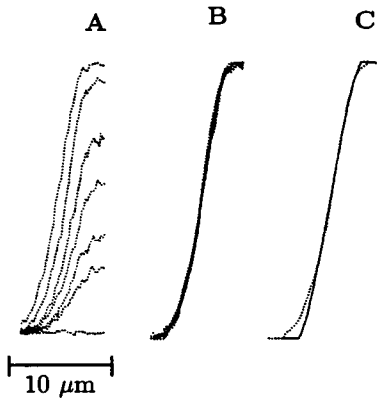

FIGURE 3 Optical linespread function. Determination of "space constant," Λ, for optical linespread function. (*A*) Scans of fluorescence image across proximal end of cell (shaded portion of scan area 2, Fig. 4 *A*). Time points:0:01 (background), 0:36, 1:04, 2:14, 4:37, 10:13, and 18:37 after whole-cell access. (*B*) Normalized scans from *A* (not including background scan). Scans digitally filtered (Gaussian with SD of 1.0 μm). Background was subtracted and each scan was normalized by its maximum value. The scans were translated horizontally so that the half-maximal values coincide. (*C*) Unit step convolved with optical linespread function, $\mathscr{L}_\Lambda$ (Eq. 8), sp-const = 2.4 μm (*solid trace*), overlaid on mean of traces from *B* (*dotted trace*). Cell FC6.

We also examined the transverse distribution of fluorescence at several points along the length of the outer segment. Radial scans were made at each of the three points (*a*, *b*, *c*) shown in Fig. 4 *A*. We fit each scan according to Eq. 7, and convolved the resulting profile with the optical linespread function (Eq. 5), using the space constant determined as described above (section Optical Linespread Function). At each position, the fluorescence scans (*dotted traces*, Fig. 4 *C*) are bilaterally symmetric, as one would expect. The slight overshoot of the fitted trace at the peak, and slight undershoot at the skirt, could be due either to optical blurring in the z direction or to tight adhesion of the outer segment to the substrate, causing distortion of the presumed circular cross-section. Similar results were found in all cells for which this analysis was performed (N = 6, three CF and three fl-cGMP). These results confirm that equilibration along the transverse axis of the outer segment occurs rapidly relative to the time required for longitudinal equilibration, affirming the validity of the one-dimensional diffusion model.

Determination of the tortuosity factor

Figs. 5 and 6 show electron micrographs of outer segment discs in cross-section at low and high magnifications, respectively. Fig. 5 shows a typical pattern of incisures. The higher magnification of Fig. 6 shows most clearly that the cytoplasm is constrained to two narrow spaces: 1) the margin between the plasma membrane and the disc membrane, and 2) the incisures in the discs themselves.

[2] The optical linespread function, rather than the point spread function, can be used here since transverse scans were taken over a narrow slice of the x axis in which fluorescence intensity was effectively constant.

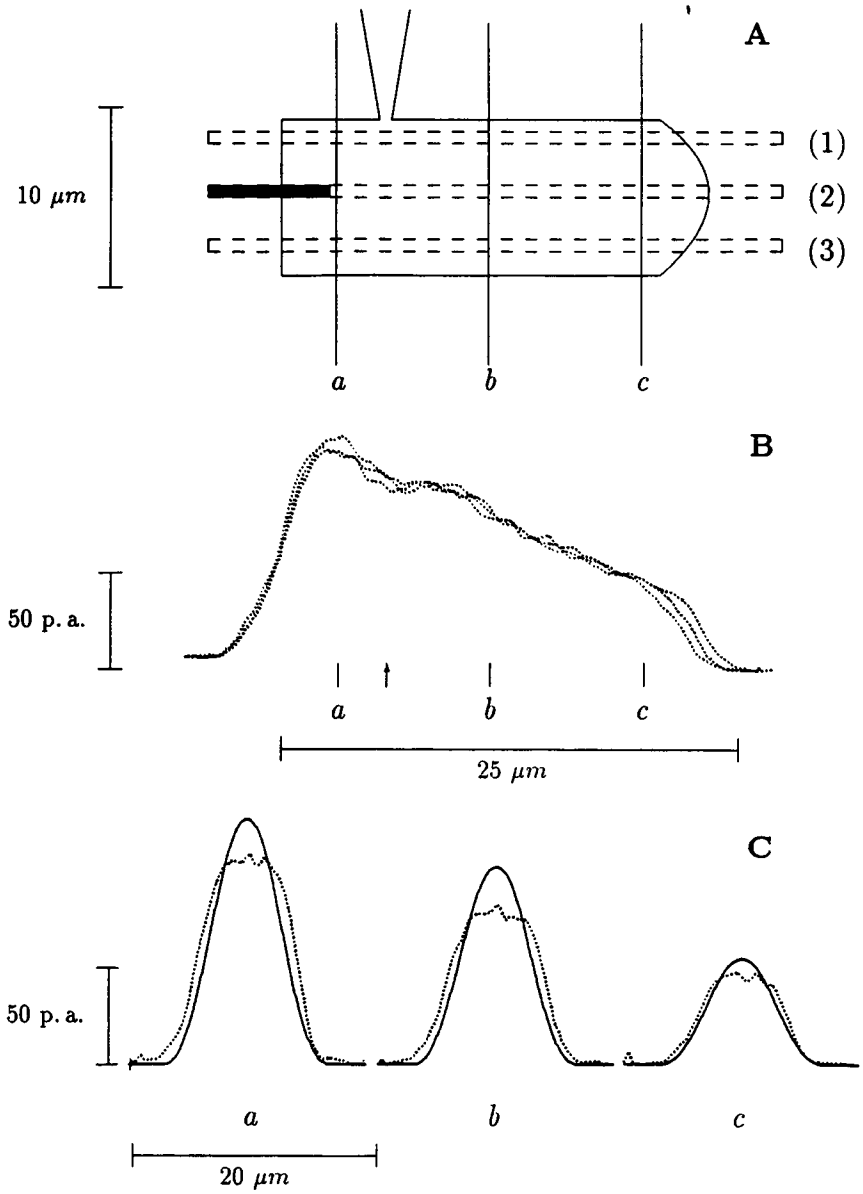

FIGURE 4 Demonstration of radial isotropy. (*A*) Schematic diagram showing locations of pipette, longitudinal scan areas (*dashed boxes*), and radial scan lines (*a*, *b*, *c*). Filled area at left of center scan box shows location of edge scan used in Fig. 3. (*B*) Scans of the three areas, 1–3, indicated in *A*, spatially averaged parallel to the long axis of the outer segment. Scale factors for each scan area were: (*1*) 1.3, (*2*) 1.0, (*3*) 1.15, in good agreement with the expected differences in path length for the three areas. The scans differ in length due to the curved profile of the distal tip. Arrow indicates pipette location. (*C*) Radial scans (*dotted traces*) from positions *a*, *b*, and *c*, overlaid with fitted traces (*solid lines*), derived from Eq. 7. The scale factor, *S*, was obtained from the best-fitting solution for the longitudinal diffusion profile; the outer segment radius, *r*, was measured from the video record; the dye concentration, C_x, at each position was allowed to vary ±5% from the fitted longitudinal profile, to allow for the noise in the measured fluorescence trace. Cell FC6, 2:14 after whole-cell access; fluorescence image averaged over 16 frames (500 ms); traces digitally filtered (Gaussian with SD of 1.2 μm).

The total length of the cytoplasmic rim and incisures was measured in three separate electron micrographs of salamander discs; results are presented in Table 1. The average width (mean ± SE) of the incisures and of the gap at the cytoplasmic rim was found to be 10.8 ± 0.7 nm. Assuming that any shrinkage of the tissue due to fixation was uniform for the entire cross-section, we calculated the patent cross-sectional area, F_A, (i.e., the area available for longitudinal diffusion), to be 1.4% of the total outer segment cross-section. The cytoplasm occupies about half of the total outer segment volume (Blaurock and Wilkins, 1969; Gras and Worthington, 1969; Rosenkranz, 1977), i.e., F_V = ½. Thus, we obtain a value of 0.028 for F_A/F_V, the "tortuosity" factor for hindrance of longitudinal diffusion by the disc stack ((Lamb et al., 1981), cf. Eq. A13).

TABLE 1 Patent cross-sectional area of salamander discs

#	Total length		Patent area*	F_A‡
	Rim	Incisures		
	μm		μm²	
1	38	81	1.3	0.014
2	37	78	1.3	0.014
3	33	83	1.3	0.014

*Mean width of incisures: 0.011 μm.
‡Total cross-sectional area: 95 μm².

Longitudinal diffusion results: CF cells

General description

The measured fluorescence intensity and the best-fitting theory traces for two outer segments infused with CF are presented in a two-dimensional format in Fig. 7 and in a three-dimensional format in Fig. 8. Presentation in two dimensions facilitates comparison of the measured and pre-

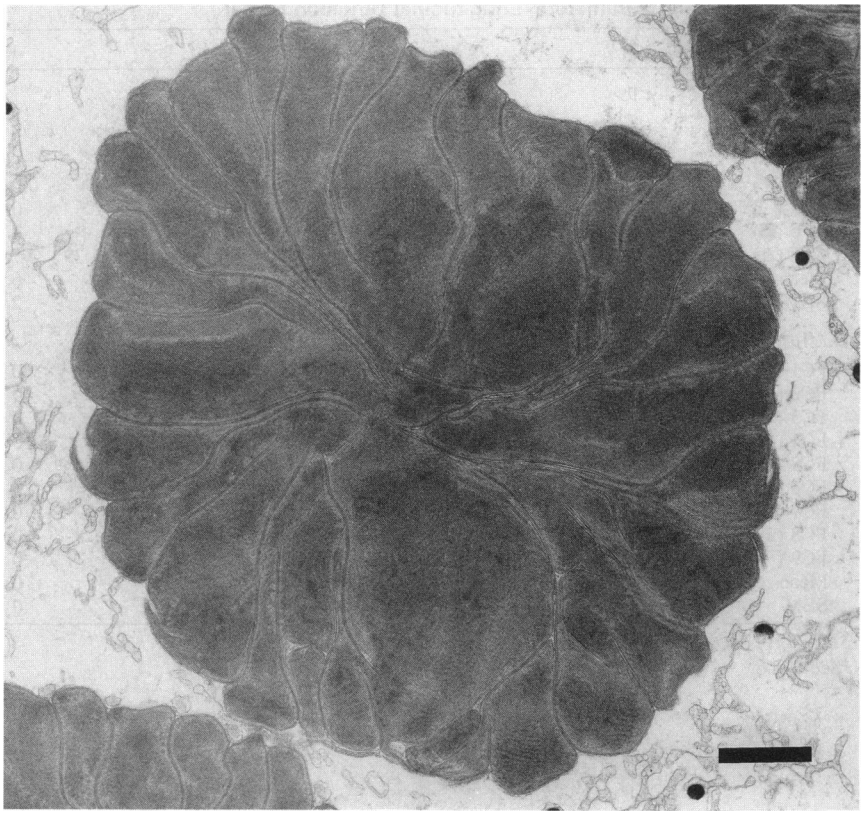

FIGURE 5 Salamander disc cross-section. Electron micrograph of salamander disc in cross-section, showing pattern of the incisures. Scale bar: 2 μm. (Micrographs courtesy of Dr. A. P. Mariani of the NIH.)

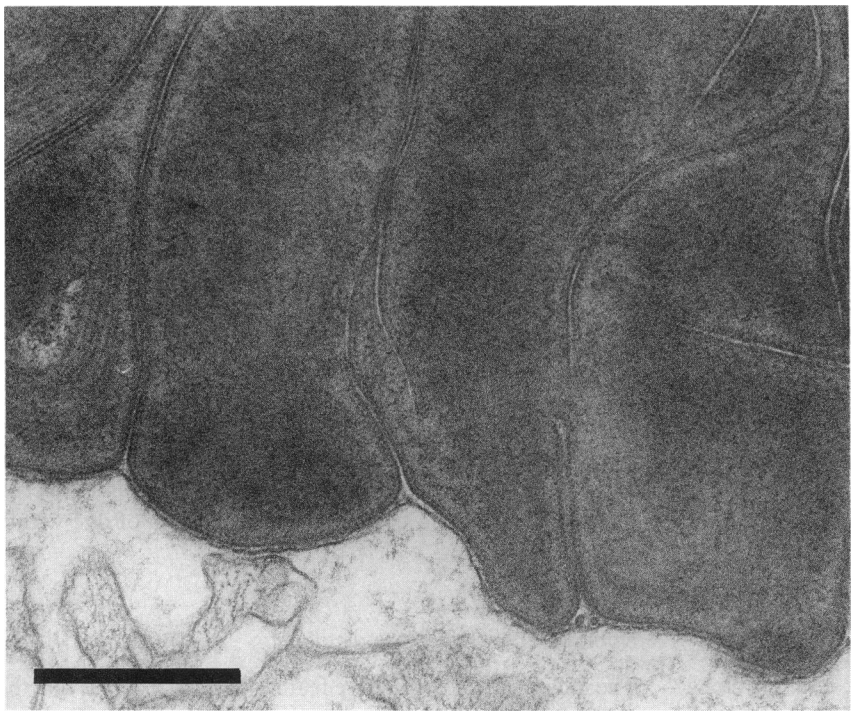

FIGURE 6 Salamander disc cross-section, high magnification. High-magnification view of a salamander disc, showing that the cytoplasm is constrained to the gap between the disc and the plasma membrane and to the narrow incisures. Scale bar: 0.5 μm. (Micrographs courtesy of Dr. A. P. Mariani.)

dicted fluorescence profiles, while the three-dimensional format shows more clearly the progression of the diffusion process in time. In Fig. 7, the unbroken lines show the measured fluorescence intensity above background at the times indicated in the figure legend (some experimental time points are omitted for clarity). The dotted lines show the fluorescence intensity predicted from the longitudinal diffusion model at the corresponding time points. The arrows indicate the pipette location. The upper panel shows the results for a typical carboxyfluorescein cell; the estimated effective longitudinal diffusion coefficient was $D_x = 2.1\ \mu m^2 \cdot s^{-1}$. The lower panel shows the results for the cell that yielded the lowest estimated

TABLE 2 Best-fit Parameters, Longitudinal Diffusion Model

Cell	F_∞*	τ_1	τ_2	τ_3	ν_L	χ	D_x	E_{RMS}‡
A. CF cells	p.a.	ms	s	s	$s^{-1} \times 10^3$	$\times 10^3$	$\mu m^2 \cdot s^{-1}$	
CF1 (○)	47	0.2	0.002	53.8	18.62	6.90	3.5	12.9
CF2 (●)	51	1.0	0.002	173	5.39	4.85	2.1	10.5
CF3 (▽)	90	0.2	0.002	8.8	8.18	3.21	1.6	10.4
CF4 (▼)	117	9.9	97.1	324	0.74	4.95	2.5	5.5
CF5 (□)	127	0.2	0.002	255	0.60	4.50	2.3	11.4
CF6 (■)	236	0.2	47.2	46.3	1.71	0.31	0.2	5.5
CF7 (△)	317	1.1	0.003	500	7.88	2.40	1.2	10.2
Mean					6.16	3.76	1.9	9.5
SEM					2.60	0.85	0.4	1.2
B. fl-cGMP cells								
FC1 (○)	205	2.1	0.002	112	0	0.63	0.2	8.2
FC2 (●)	294	4.3	0.005	543	0	5.85	2.2	12.3
FC3 (▽)	75	0.3	0.002	56	0	0.90	0.3	11.5
FC4 (▼)	166	2.0	0.002	133	0	0.97	0.4	9.6
FC5 (□)	180	4.4	0.005	181	0	4.70	1.8	9.9
FC6 (■)	186	0.2	0.002	190	0	3.41	1.3	11.2
FC7 (△)	184	0.3	0.002	240	0	2.28	0.9	9.9
FC8 (▲)	188	0.9	0.002	40	0	1.64	0.6	10.8
FC9 (◇)	78	98900	111	129	0	2.53	1.0	11.1
Mean					0	2.55	1.0	10.5
SEM					0	0.68	0.2	0.4

*$F_\infty = \mathcal{F}(p,\infty)$, see Eqs. 4 and 5.
‡See Eq. 6.

longitudinal diffusion coefficient of all CF cells, $D_x = 0.2$ $\mu m^2 \cdot s^{-1}$. The mean effective longitudinal diffusion coefficient (mean ± SE) for the seven CF cells was 1.9 ± 0.4 $\mu m^2 \cdot s^{-1}$. The model parameters and results for all CF and fl-cGMP cells are tabulated in Table 2.

The spatial distribution of fluorescence intensity over time is illustrated for the same two CF cells in three-dimensional format in Fig. 8. Each row of this figure shows the measured fluorescence intensity (*left panel*), the best-fitting theoretical profile (*center panel*), and the residuals (*right panel*) for a single cell. The data are presented as 3-dimensional surface plots, with x and time plotted on the x and y axes, respectively (vice versa for cell CF6), and fluorescence intensity plotted on the z axis. The residuals are plotted at the same scale as the first two graphs, but with the z axis offset to make negative residuals visible.

There are four general features of the CF data (as seen in Figs. 7 and 8) for which a satisfactory longitudinal diffusion model must provide an account: 1) the gradual increase in fluorescence intensity in the cell at the pipette position; 2) the time course of the increase in fluorescence at points distal to the pipette; 3) the striking nonuniform distribution of fluorescence at long times after whole-cell access; and, 4) at long times, the continued increase in overall fluorescence with little change in the shape of the fluorescence profile. In the model, each of these four features is determined by one or more of the parameters discussed above in the Theory section. Thus, feature 1 is captured primarily by the temporal forcing function, $\Phi(t)$; feature 2 by the effective longitudinal diffusion coefficient, D_x; feature 3 by the loss constant, ν_L; and feature 4 by the binding ratio, B. The effect of each of these parameters on the model's behavior is discussed below.

Figs. 7 and 8 show that the model provides an adequate description of the CF fluorescence profiles. In particular, the theoretical traces are in good agreement with the measured fluorescence profiles during the time when the fluorescence intensity is changing most rapidly along the length of the outer segment. It is this portion of the data that is most critical in determining D_x for the cell in question.

For both cells in Figs. 7 and 8, the predicted fluorescence falls short of the measured fluorescence at very early times (first trace at 0:46 after whole-cell access for cell CF2, first two traces at 0:05 and 0:10 for cell CF6). This may reflect a nondiffusional process such as a rapid initial pressure change resulting from the rupture of the membrane patch at the initiation whole-cell access. Any effects of such a process appear to damp out rapidly, and have no discernible effect on the subsequent diffusion of dye within the outer segment.

Nonuniform steady-state distribution

The most striking qualitative feature of the CF data is that the steady-state distribution of fluorescence is not uniform. At long times, fluorescence intensity steadily decreases along the x axis, at increasing distance from the pipette position. This phenomenon is not due to a longitudinal asymmetry in the rod outer segment, as it was seen when the electrode attachment was made at either the proximal (inner segment) or the distal (disc-shedding) end of the outer segment.

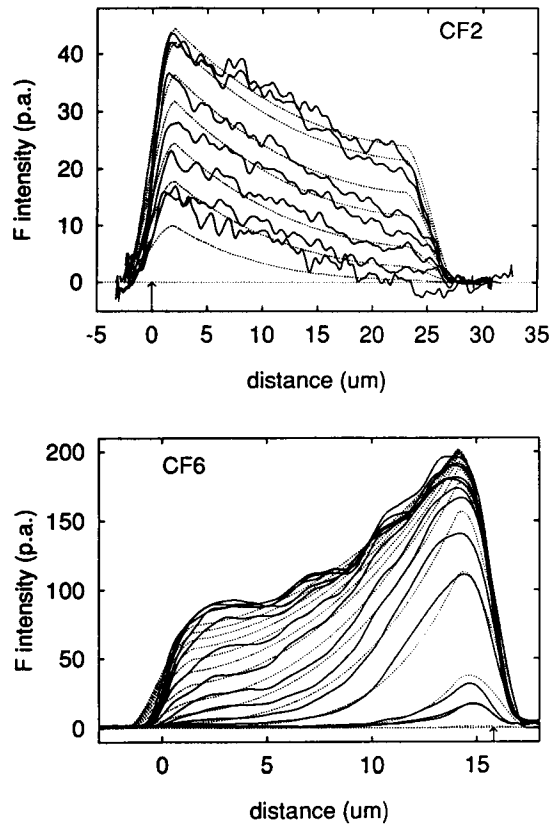

FIGURE 7 CF longitudinal diffusion, 2-dimensional plots. Traces show measured fluorescence above background (*unbroken, wavy lines*) and predicted fluorescence from longitudinal diffusion model (*dotted lines*) for two cells. (Baseline of zero p.a. is also shown with the *dotted line*.) Arrows show position of the whole-cell pipette. For clarity of presentation, only selected time points are shown here. Cell CF2, time points 0:46, 1:28, 2:13, 3:21, 4:23, 6:35, and 8:25 after whole-cell access. Cell CF6, time points 0:05, 0:10, 0:50, 1:54, 2:56, 3:55, 4:50, 5:56, 6:53, 7:54, 8:55, 9:56, 10:57, 12:10, and after whole-cell access. Note that very little change in fluorescence profile occurs in the last 2–3 min.

The loss rate constant, v_L

A diffusion model that does not include a loss of dye cannot account for the observed steady-state distribution of CF. With the loss parameter, v_L, removed, the fitting behavior of the model was qualitatively poorer. With $v_L = 0$, the best-fitting value of D_x was decreased 1.6-fold, on average, from the best-fitting value of D_x with v_L free to vary. The lower diffusion coefficient resulted in a large, systematic increase in error at early times in the region of the outer segment distal to the pipette. The reduced D_x also led to an increase in the predicted time to equilibrate; i.e., with $v_L = 0$, the least error was produced by fitting the nonuniform steady-state of the fluorescence data with a slowed rise to an eventually uniform distribution.

Possible mechanisms for loss of dye include photodestruction, leakage of dye across the cell membrane, and enzymatic destruction (as occurs for cGMP). Our estimates of the rate of CF photodestruction (see Methods) argue against photodestruction, as does the fact that fl-cGMP showed a homogeneous steady-state distribution (see Figs. 9 and 10). Leakage of CF across cell membranes, however, has been reported (Rink et al., 1982).

We were not able to measure directly the rate of loss of CF with the pipette attached, since the pipette provided a constant source of dye. Several attempts were made to withdraw electrodes from cells in order produce the desired initial condition, but the cells invariably suffered damage that led to an immediate loss of fluorescence.

Effects of binding

At long times after whole-cell access, fluorescence intensity appears to increase almost uniformly along the entire length of the outer segment (cf. Fig. 8 for times longer than ~6 min); i.e., the overall fluorescence increases, but

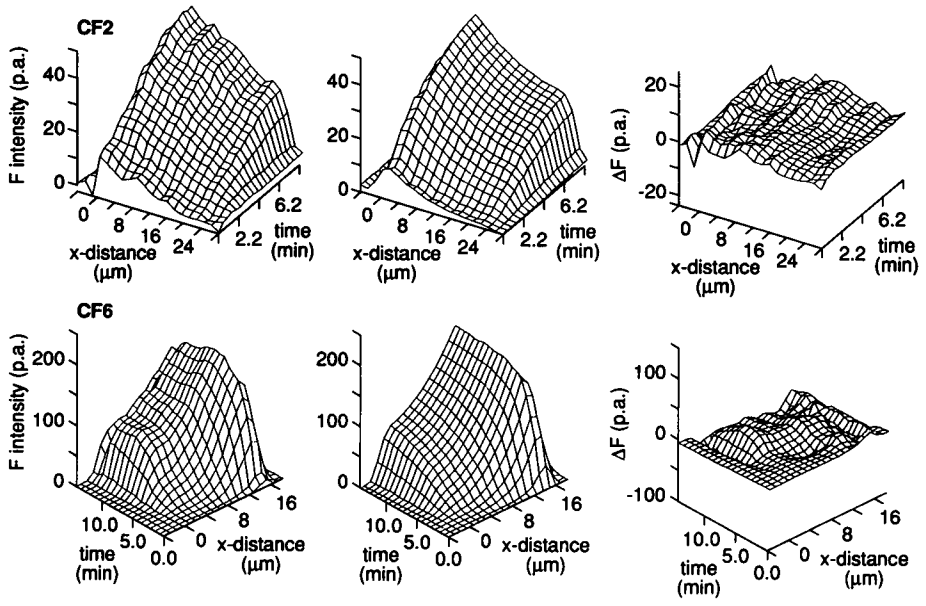

FIGURE 8 CF longitudinal diffusion 3-dimensional surface plots of (left to right): measured fluorescence intensity (above background), fitted fluorescence intensity (Eq. 5), and residuals (measured minus fitted fluorescence). Top row, cell CF2, bottom row, cell CF6. (Note: for cell CF6, the x and t axes are reversed relative to those for cell CF2.)

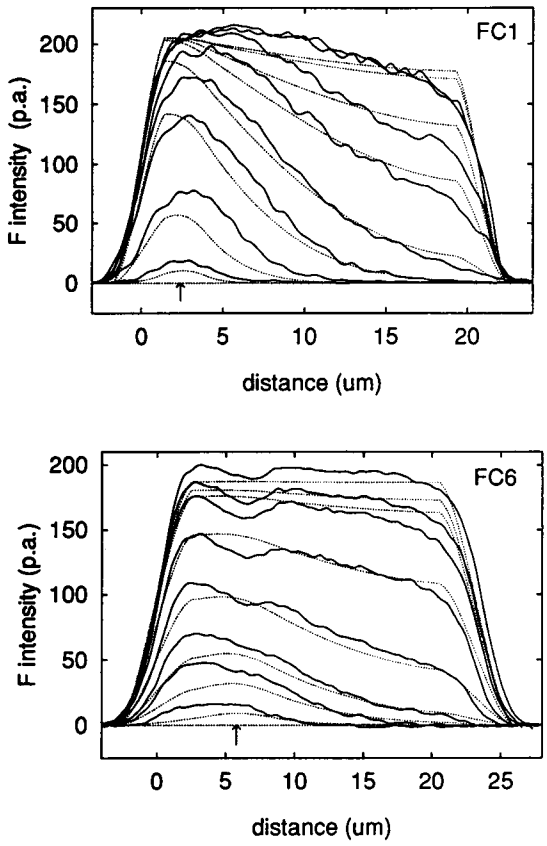

FIGURE 9 fl-cGMP longitudinal diffusion, 2-dimensional plots. Traces show measured fluorescence above background (*solid lines*) and predicted fluorescence from longitudinal diffusion model (*dotted lines*). (Baseline of zero p.a. is also shown with *dotted line*.) Arrows show pipette location. For clarity of presentation, only selected time points are shown here. Cell FC1, time points 0:08, 0:37, 2:03, 4:10, 8:25, 12:42, 19:32, and 21:25 after whole-cell access. Cell FC6, time points 0:11, 0:36, 1:04, 2:14, 4:37, 10:13, and 18:37 after whole-cell access.

the distribution of fluorescence is relatively unchanged. This phenomenon can be explained if a large fraction of the dye in the outer segment is bound; at long times after whole-cell access, additional dye entering the cell from the pipette represents a decreasingly small fraction of the total dye (free and bound), and the total fluorescence intensity can appear to increase uniformly. Calculations with the theoretical model bear out this interpretation; without the inclusion of binding in the model, no other parametric variations can account for the phenomenon of overall fluorescence increase at long times. We emphasize that the binding ratio parameter B is well constrained by its dual and reciprocal effects: retarding diffusion (Eqs. 3 and A13), and accounting for the long-term increase in fluorescence (Eq. 4).

Longitudinal diffusion results: fl-cGMP cells

General description

The measured fluorescence intensity profiles (*solid lines*) and the best-fitting theory traces (*dotted lines*) for two outer segments infused with fl-cGMP are presented in two-dimensional format in Fig. 9 and in three-dimensional format in Fig. 10. The mean effective longitudinal diffusion coefficient (mean ± SE) estimated for the nine fl-cGMP cells was $1.0 \pm 0.2\ \mu m^2 \cdot s^{-1}$. The cell in the upper panel in Figs. 9 and 10 yielded the estimate $D_x = 0.2\ \mu m^2 \cdot s^{-1}$; the cell in the lower panel gave $D_x = 1.3\ \mu m^2 \cdot s^{-1}$.

As was the case for cells infused with CF, the fluorescence intensity at the pipette location increased gradually over time. The time course of the increase in fluorescence intensity distal to the pipette also was similar for the CF and fl-cGMP cells. In marked contrast to the results from the CF cells, however, the fl-cGMP cells had approximately uniform distributions of fluorescence intensity at long times after

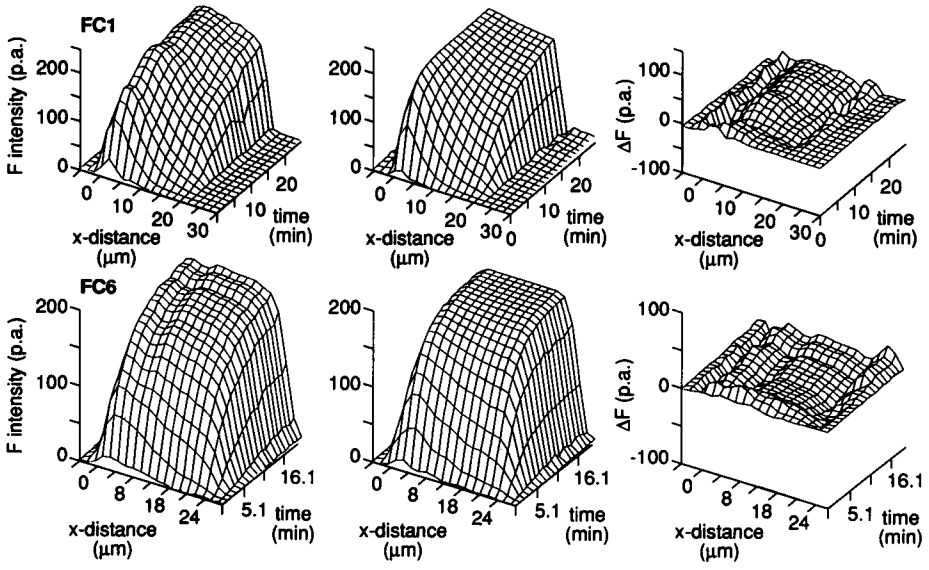

FIGURE 10 fl-cGMP longitudinal diffusion, 3-dimensional surface plots of (left to right): measured fluorescence intensity (above background), fitted fluorescence intensity (Eq. 5), and residuals (measured minus fitted fluorescence). Top row, cell FC1; bottom row, cell FC6.

whole-cell access (see Figs. 9 and 10). For each of the nine fl-cGMP cells, the theoretical traces fit the measured fluorescence intensity profiles best when the loss rate constant, ν_L, was set equal to zero.

Model parameters

The validity of the use of the temporal forcing function, $\Phi(t)$, and the effect of the tortuosity factor, χ, on the behavior of the longitudinal diffusion model are now examined.

The temporal forcing function, $\Phi(t)$

The temporal forcing function (Eq. A9) "drives" the model by setting the boundary condition at the location of the pipette. But does the temporal forcing function yield a reasonable approximation for this boundary condition, or is it just an arbitrary function which happens to give the least global error? The results presented in Fig. 11 answer this question.

In Fig. 11, the time course of the temporal forcing function for each cell (*solid traces*) is compared with the time course of the normalized fluorescence intensity at the pipette position (symbols as in Table 2). The top row shows the data from the CF cells, and the bottom row shows the data from the fl-cGMP cells. The fluorescence data have been normalized to the theoretical maximum fluorescence (F_∞), which is the predicted fluorescence at the pipette position at long times after whole-cell access ($F_\infty = \mathcal{F}(p,\infty)$; see Eqs. 4 and 5). Although the parameters for the temporal forcing functions (τ_1-τ_3) were obtained with a fitting routine that sought to minimize the *global* error between the measured fluorescence data and the fluorescence profile predicted from theory, the temporal forcing functions agree well with the *local* fluorescence data at the pipette position.

To determine if the value of D_x was dependent on the temporal forcing function, we measured the correlation between the fitted effective longitudinal diffusion coefficient, D_x, and $\tau_1 + \tau_2 + \tau_3$, the sum of the time constants of the temporal forcing function. The linear regression correlation coefficient was 0.279 (not significantly different from zero), and the slope of the regression line was 0.0016. Thus, there is no evidence that our estimates of D_x are affected systematically by the temporal forcing function.

Variation of the retardation factor χ

The sensitivity of the model to the parameter χ (Eq. A13) was evaluated for each cell. χ was systematically varied from its best-fit value, while holding the other parameters (τ_1–τ_3, S, ν_L) fixed at their best-fit values. E_{RMS} (see Eq. 6) could then be examined as a function of χ. Since D_x is directly proportional to χ, the data are presented in terms of D_x, the effective longitudinal diffusion coefficient. In the top row, E_{RMS} is shown as a function of D_x for each cell (CF cells are on the left; fl-cGMP cells are on the

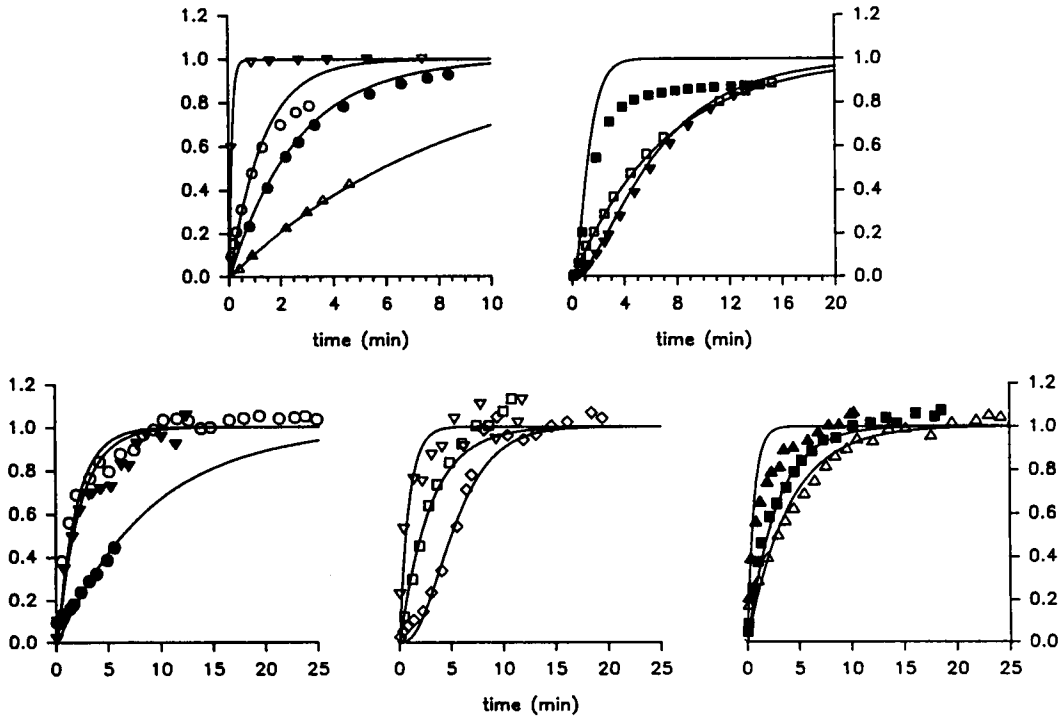

FIGURE 11 Temporal forcing functions. The symbols in each panel show the time course of fluorescence intensity (above background) in the region immediately beneath the pipette tip. The solid lines show the time course of $\Phi(t)$, the temporal forcing function, for each cell. Top row, CF cells; bottom row, fl-cGMP cells. Note different time scales. Symbols are as in Table 2.

right). Each curve in the upper part of Fig. 12 is a profile of the minimum E_{RMS} projected on the *single* dimension D_x.

In the bottom row, the same data are presented in a simpler format. For each cell, a line segment is plotted that shows the range of diffusion coefficients for which the model produced a set of fluorescence intensity profiles with an error $\leq 1.5 \times E_{RMS}$ of the best-fit set of profiles. The symbols used to identify the cells are the same as in Table 2.

Dye binding

The parameter χ lumps together three factors that tend to slow longitudinal diffusion in the outer segment: 1) tortuosity, 2) viscosity of the outer segment cytoplasm, and 3) binding of the dye to relatively immobile sites (see Theory, Eq. A13). Substituting Eq. A13 into Eq. 3 and rearranging yields:

$$B = \frac{F_A D_{aq}}{\eta F_V D_x}. \quad (9)$$

Our measurements of F_A (Fig. 6 and Table 1), combined with previous structural studies of the outer segment, predict the value of $F_A/F_V = 0.028$. In order to put an upper limit on B, η was set to 1.3, the lowest reported value for cytoplasmic viscosity (Fushimi and Verkman, 1991). Taking $D_{aq} = 380\ \mu m^2 \cdot s^{-1}$ as the aqueous diffusion coefficient for fl-cGMP ($D_{aq} = 480\ \mu m^2 \cdot s^{-1}$ for CF) (Longsworth, 1953) yields the values $B = 8.6$ for fl-cGMP and $B = 5.4$ for CF; that is, fl-cGMP is predicted to be 90% bound, and CF to be 84% bound.

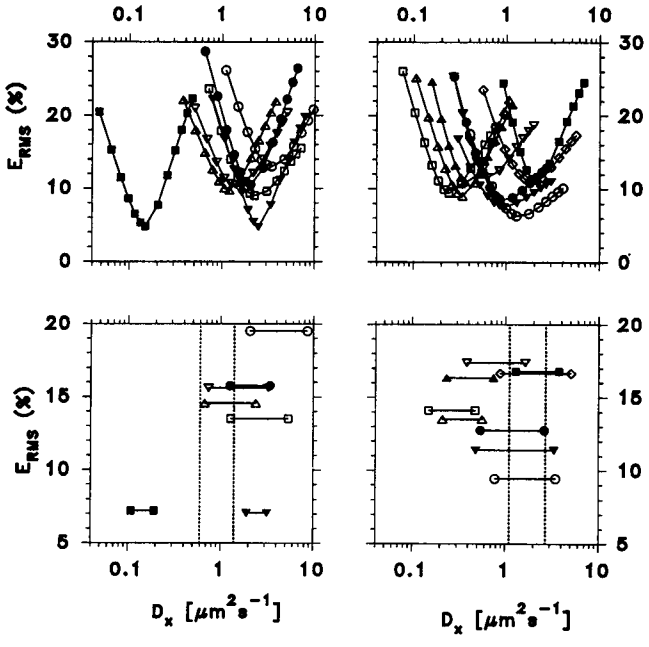

FIGURE 12 E_{RMS} as a function of D_x. For each cell, all model parameters except χ were held fixed at their best-fit values; χ was systematically varied from 0.1–2.5 × its optimum value. Top row, E_{RMS} is plotted as a function of D_x (note logarithmic scale) for each cell. Left, CF cells; right, fl-cGMP cells. Symbols as in Table 2. Bottom row, same data as above, but here only the width of the curve is shown for an increase in E_{RMS} of 50% from the best-fit value. Dotted lines delineate the range of the mean ± 2 SE of D_x for the two groups of cells.

TABLE 3 Summary of effective longitudinal diffusion coefficients

	M_r	D_{aq}	B	D_x
		$\mu m^2 \cdot s^{-1}$		$\mu m^2 \cdot s^{-1}$
CF	376	480	5.4	1.9
fl-cGMP	764	380	8.6	1.0
cGMP	345	494	2–6	1.4–5.5

A similar degree of binding has been reported for Fura-2, the calcium indicator dye. Measurements of Fura-2's fluorescence emission anisotropy and absorbance spectrum indicate that from 60 to 80% of the dye is bound by soluble myoplasmic proteins, including glycolytic enzymes (Konishi et al., 1988). The degree of binding was found to decrease with increasing ionic strength, indicating that charge interactions were important in the binding reaction. Although Fura-2 is more highly charged[3] than either fl-cGMP or CF, nonspecific binding to proteins or lipids in the outer segment seems plausible.

Estimation of D_x for cGMP

By assuming that the diffusion of cGMP in the outer segment is governed by the same factors that govern diffusion of the two dyes, we can derive an estimate for $D_{x,cGMP}$, the effective longitudinal diffusion coefficient of cGMP. Specifically, we assume that the tortuosity factor, F_A/F_V, and the cytoplasmic viscosity, η, governing longitudinal diffusion are the same for all three compounds. It follows that the factor χ, which relates the free aqueous diffusion coefficient to the effective longitudinal diffusion coefficient (Eqs. 3 and A13), differs for the three compounds only in the degree of binding. Thus, we can derive the relationship

$$D_{x,cGMP} = D_{x,dye} \times \frac{B_{dye}}{B_{cGMP}} \left[\frac{M_{dye}}{M_{cGMP}}\right]^{1/3} \quad (10)$$

from Eqs. 3 and A13 and the Stokes Law formula for the diffusion coefficient of a spherical particle where M_{dye} and M_{cGMP} are the masses of the dye and cGMP, respectively, assumed to have the same density. Our results provide estimates of B_{dye} for the two fluorescent compounds. Substituting $B_{cGMP} = 1$ in Eq. 10 (i.e., assuming no effective cGMP buffering) gives the upper limits for $D_{x,cGMP}$ predicted from the dye diffusion measurements. Using the values of $D_{x,dye}$, B_{dye}, and MW (see Table 3) for CF, the equation yields an upper limit of $D_{x,cGMP} = 10.5\ \mu m^2 \cdot s^{-1}$; substituting the values for fl-cGMP yields $D_{x,cGMP} = 11.2\ \mu m^2 \cdot s^{-1}$. A "lower limit" may be obtained by assuming that $B_{cGMP} = B_{fl\text{-}cGMP}$,

[3] The dye exists mostly as pentavalent anions under the conditions of Konishi et al. (1988).

in which case we obtain $D_{x,cGMP} = 1.2\ \mu m^2 \cdot s^{-1}$. We thus believe, on the basis of the data presented here alone, that $D_{x,cGMP}$ lies between 1 and 11 $\mu m^2 \cdot s^{-1}$.

The actual value of $D_{x,cGMP}$ in the rod will depend on the extent and kinetics of cGMP binding, primarily to low-affinity binding sites. Based on considerations of biochemical data on the high-affinity cGMP binding sites, the amount of total extractable cGMP and the amount of free cGMP in the dark resting state,[4] Lamb and Pugh (1992) estimated $B_{cGMP} = 2$. A recent biochemical binding study (Cote and Brunnock, 1993) provides evidence that there is a class of low-affinity binding sites for cGMP that could raise B_{cGMP} as high as 6. Using these values ($B_{cGMP} = 2,6$) in Eq. 10, we obtain, respectively, $D_{x,cGMP} = 1.4\ \mu m^2 \cdot s^{-1}$ and $D_{x,cGMP} = 5.5\ \mu m^2 \cdot s^{-1}$. A summary of the effective longitudinal diffusion coefficients for CF, fl-cGMP, and cGMP, is presented in Table 3. The possible effects of binding on cGMP diffusion are considered further in the Discussion section.

DISCUSSION

Necessity and sufficiency of a one-dimensional diffusion model

The results presented here using fluorescent probes confirm what has been expected on theoretical (Lamb et al., 1981) and indirect empirical (Baylor et al., 1979) grounds: longitudinal diffusion of substances in the rod outer segment is greatly hindered by the presence of the discs, and the time for longitudinal equilibration is very much greater than the time for radial equilibration (Fig. 4). Thus, any model of processes in the outer segment that effectively postulates longitudinal gradients of diffusible substances must incorporate explicitly the effects of diffusion in the longitudinal dimension, though (on the time scale relevant to longitudinal equilibration) the model need not include radial diffusion.

Time to equilibration

In addition to its great utility for controlling membrane potential, the whole-cell recording technique has proved invaluable as a tool for introducing a great variety of nonpermeant molecules into cells. Substances introduced into photoreceptors via whole-cell electrodes have led to major advances in the understanding of the processes underlying phototransduction and light adaptation; such substances include cGMP (Cameron and Pugh, 1990), BAPTA (Torre et al., 1986), aequorin (McNaughton et al., 1986), ATP and GTP (Sather and Detwiler, 1987).

The analysis of experiments in which substances are introduced into cells via whole-cell electrodes generally requires the assumption that the substances are distributed uniformly. Experiments with fluorescent probes, however, show that the time to achieve equilibration between pipette and cell interior can be many seconds to minutes (Pusch and Neher (1988), cf. Fig. 13, below), and also show that the substances are often distributed in a spatially inhomogeneous manner, due to cell compartmentalization, differential destruction, or leaks.

The whole-cell recording technique is not the sole technique that has been used to introduce substances into rod outer segments. Many experiments have also been performed on *truncated* rod outer segments held in suction pipettes (Yau and Nakatani, 1985; Nakatani and Yau, 1988; Kawamura and Murakami, 1989). Because substances introduced from one end of a truncated rod must enter through the cytoplasmic rim and incisures of the initial disc, and because all factors restricting longitudinal diffusion in whole outer segments also are present in truncated rods, it can be expected that the time for substances to equilibrate longitudinally in truncated outer segments will be comparable to the time taken for equilibration in whole-cell recording.

Our results provide a figure of merit for the "equilibration time" that should be useful for characterizing experiments in which substances are introduced into single rods via whole-cell pipettes or into the open end of a truncated rod preparation. For the rods of our experiments into which fl-cGMP was introduced, a uniform distribution of dye was achieved at long times, and thus the integrated whole-cell fluorescence can be used to estimate equilibration time. The net mass of dye transferred into the cell by time t is proportional to the whole-cell fluorescence at time t, and the equilibrated distribution is well characterized by F_∞, the theoretical estimate of the fluorescence intensity maximum. Thus, we define the time course of normalized whole-cell fluorescence, $\bar{F}_{wc}(t)$, by:

$$\bar{F}_{wc}(t) = \frac{1}{LF_\infty} \int_0^L F(x,t)\, dx. \qquad (11)$$

For each of the nine outer segments into which fl-cGMP was introduced, $\bar{F}_{wc}(t)$ was calculated, by numerical integration over x, for each time point for which data were available. The results are plotted in Fig. 13. The unbroken lines are the best fitting single exponentials for the two curves at the extremes of the distribution. The respective time constants of these curves are 3.4 and 7.7 min. Thus, a figure of merit for the equilibration time for small molecules introduced into the outer segment from an infinite point source is 3–8 min; the average equilibration time was 6.0 min.

The equilibration time for any particular substance of course, will depend on the degree of intracellular binding to relatively immobile sites of the molecule in question. If the molecule introduced is relatively less bound than fl-cGMP, equilibration with the pipette would be reached more rapidly. To the extent that intracellular binding is nonspecific (Konishi et al., 1988), the equilibration time for a small, charged molecule would likely be similar to that for fl-cGMP. For example, the equilibration time for

[4] The buffering that is obtained in the dark resting state is not to be confused with the issue of cGMP buffering under bright light conditions, when the decline in free cGMP exposes a number of high-affinity sites (reviewed in Pugh and Lamb (1990)).

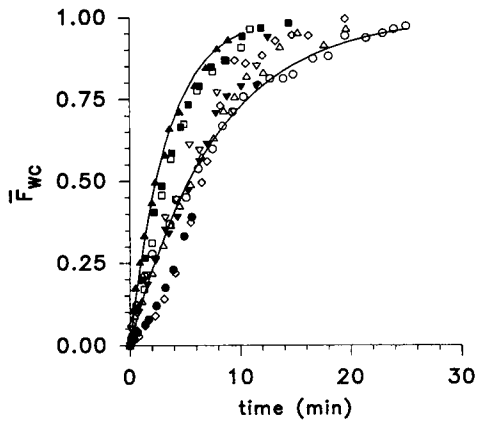

FIGURE 13 Equilibration time. Each symbol represents the normalized whole-cell fluorescence, $\bar{F}_{wc}(t)$ (Eq. 11), for an individual fl-cGMP cell at the indicated time after whole-cell access (symbols as in Table 2). The solid lines show the best least-squares fit of $1 - \exp(-t/\tau)$ for the two cells at the extremes of the distribution, FC8 (▲, τ = 3.4 m) and FC1 (○, τ = 7.7 m).

cGMP would be expected to be ~2–3 min, if, as has been estimated (Lamb and Pugh, 1992), B_{cGMP} = 2. Larger molecules, such as proteins, would be expected to equilibrate much more slowly.

In the case in which substances introduced into rods undergo some kind of loss as they diffuse, the steady-state distribution will be nonuniform. We have argued that leakage of CF across the outer segment membrane is the likely cause of the nonuniform steady-state distributions; such leakage is consistent with other experiments involving the diacetate ester of CF (Rink et al., 1982). Formally, the effect of destruction during diffusion is equivalent to the loss of dye through leakage (cf. Eq. 2). In this context, it is noteworthy that both cGMP and GTP, when introduced into the outer segment from a point source, must diffuse in the presence of active degradative enzymes. A necessary consequence of this "diffusion with destruction" is that uniform distributions of these substances cannot be achieved unless further steps are taken, such as inhibition of the degradative enzymes (cf. use of the PDE inhibitor, IBMX, in (Nakatani and Yau, 1988)). It should also be noted that the cGMP moiety of fl-cGMP is hydrolyzed extremely slowly by PDE—at least 10,000 times more slowly than cGMP itself (Caretta et al., 1985). Thus, PDE is not expected to affect fl-cGMP diffusion.

cGMP binding sites and diffusion

Our modeling results suggest that fl-cGMP is bound to a greater degree than CF (see Table 3). Since both dyes possess almost identical chromophore moieties (cf. Fig. 1), it is tempting to hypothesize that it is the cGMP moiety of fl-cGMP that causes the additional binding of this dye. This would imply the existence of a class of relatively low-affinity binding sites for cGMP. In a recent biochemical study of cGMP binding sites on PDE from amphibian rods, Cote and Brunnock (1993) found evidence for such sites, with a dissociation constant of about 7 μM and a site density of 78 μM (referenced to the water space). If, as the authors suggest, free cGMP is in rapid equilibrium with these sites, a value for B_{cGMP} of 6 in the dark resting state is predicted. This would result in an effective longitudinal diffusion coefficient of 1.8 $\mu m^2 \cdot s^{-1}$ for cGMP. Present evidence suggests that B_{cGMP} lies somewhere in the range of 2–6; further characterization of the binding kinetics of these newly discovered cGMP binding sites is needed to accurately predict their effects on diffusion of cGMP.

There has been considerable debate about the value of the Michaelis constant, K_m, of the light-activated phosphodiesterase *in situ*: measured in completely disrupted amphibian rod membranes, K_m is typically ~100 μM, whereas measured in preparations in which stacks of discs remain intact (though fully accessible to the bulk solution), K_m may be 500 μM or higher (reviewed in Pugh and Lamb (1993)). A possible account of this "K_m-shift" phenomenon has been presented by Pugh and Lamb (1993), who show that in disc membrane suspensions the cGMP concentration near the center of a disc stack is always lower than at the edge because of hydrolysis that occurs as cGMP diffuses into the stack. From the perspective of the present study, the interesting point is that a "diffusion with hydrolysis" model can account fully for the observed K_m shift of 5 or so only if the radial diffusion coefficient, D_r, of cGMP is near 100 $\mu m^2 \cdot s^{-1}$—about 5-fold lower than the aqueous diffusion coefficient of ~500 $\mu m^2 \cdot s^{-1}$. Such diminution of D_r could be due to increased viscosity, rapid binding to immobile sites, or a combination of both (see the Appendix, under *Tortuosity, viscosity, binding*). In any case, a consequence would be that the longitudinal diffusion coefficient, D_x, would also be expected to be diminished by a factor of ~4–5 below the value predicted by the effect of F_A/F_V alone. Thus, the "K_m-shift" phenomenon may provide additional evidence for an effect of binding on cGMP diffusion in the outer segment.

The longitudinal diffusion coefficient, D_x, of cGMP

Estimates of the effective longitudinal diffusion coefficient of cGMP in amphibian rods have been obtained in two previous experiments in which the spread of current along the outer segment was measured. Lamb, McNaughton, and Yau (1981) estimated an upper limit of 30 $\mu m^2 \cdot s^{-1}$ for D_x of the (then unknown) internal messenger. Recording from single toad rods with the suction electrode technique, they collected intensity-response profiles with both diffuse illumination and with narrow slits of light oriented transversely to the long axis of the rod. At very low light levels, responses to the two kinds of stimulus were similar. But as light levels were increased, the responses to slit illumination rose much less steeply than the responses to diffuse illumination. The authors interpreted their results as arising from a limitation on longitudinal spread of the internal messenger from the site of slit illumination. Their estimate of D_x, however, involved the

assumption of "total occlusion," in which the end result of photoisomerization was the complete blockage of all channels in a certain length of membrane centered on the site of isomerization. (A second model assumed an interaction of transmitter with the membrane channel having an exponential form identical to that predicted by the total occlusion model.) A recent analysis of the activation stages of phototransduction has shown that exponential saturation is a natural consequence of the cGMP cascade kinetics, and that it is very unlikely that total local occlusion occurs during the rising phase of the single-photon response (Lamb and Pugh, 1992). The estimated upper limit of 30 $\mu m^2 \cdot s^{-1}$, although not inconsistent with our results, requires caution in interpretation.

Cameron and Pugh (1990) estimated D_x for cGMP in salamander rods by analyzing the longitudinal spread of current induced by cGMP introduced from a whole-cell electrode into the inner segment of single rods. The light-sensitive current induced by the injected cGMP was measured both by the patch electrode and by a suction electrode which was holding the cell. They analyzed the time course and spatial distribution of induced membrane current with a model that included diffusion with hydrolysis of cGMP, the cable properties of the outer segment, and the voltage and [cGMP] dependence of the cGMP-activated channel. Their analysis yielded an estimate of D_x for cGMP of 6.6 ± 2.6 $\mu m^2 \cdot s^{-1}$ (mean ± SD). This estimate is closely consistent with that derived from the measurements reported here: if the buffering power for cGMP in the dark is 2 (Lamb and Pugh, 1992), the estimate of $D_{x,cGMP}$ based on the work presented here, is 5.5 $\mu m^2 \cdot s^{-1}$ (Eq. 10).

Combining the estimates made here with those obtained in experiments measuring the spread of current, we conclude that, in amphibian rods, D_x for cGMP in salamander rods lies in the range 1–11 $\mu m^2 \cdot s^{-1}$. The actual value within this range will be determined by intracellular binding of cGMP to relatively low-affinity sites.

In closing, we note that a longitudinal diffusion coefficient of 6 $\mu m^2 \cdot s^{-1}$ for cGMP in an amphibian rod has been shown sufficient to guarantee that the activation phase of the single-photon response will have the same amplification as the activation phase of the response to a more intense flash producing isotropic activation (Lamb and Pugh, 1992). Thus, it appears that the factors that control longitudinal diffusion of cGMP in the outer segment (Eqs. 3 and A13) have been so optimized that the full amplification permitted by the cGMP cascade is achieved at the single-photon level (Lamb and Pugh, 1992; Pugh and Lamb, 1993).

The authors gratefully acknowledge Dr. Andrew P. Mariani for kindly providing the electron micrographs of salamander rod outer segments used in this study.

Supported by National Institutes of Health grant EY02660.

APPENDIX

In order to solve the diffusion equation for the boundary conditions described above (see Theory section) the outer segment is treated as two compartments, one on either side of the pipette, such that $0 \le x^- \le p$ and $0 \le x^+ \le l - p$ (Fig. 2). The coordinate transformations are expressed simply:

$$x = x^- \quad \text{for} \quad 0 \le x \le p \tag{A1}$$

$$x = x^+ + p \quad \text{for} \quad p < x \le l \tag{A2}$$

The initial and boundary conditions for the problem can then be expressed in terms of x^- and x^+ as follows:

Initial

$$C(x^-, t) \equiv 0 \quad \text{for} \quad 0 \le x^- \le p, \quad t = 0; \tag{A3}$$

$$C(x^+, t) \equiv 0 \quad \text{for} \quad 0 \le x^+ \le l - p, \quad t = 0; \tag{A4}$$

Boundary

$$\partial C(x^-, t)/\partial x^- = 0 \quad \text{for} \quad x^- = 0, \quad t > 0; \tag{A5}$$

$$\partial C(x^+, t)/\partial x^+ = 0 \quad \text{for} \quad x^+ = l - p, \quad t > 0; \tag{A6}$$

$$C(x^-, t) = C_\infty \Phi(t) \quad \text{for} \quad x^- = p, \quad t > 0; \tag{A7}$$

$$C(x^+, t) = C_\infty \Phi(t) \quad \text{for} \quad x^+ = 0, \quad t > 0. \tag{A8}$$

Here, $C(x, t)$ is the concentration of (free) dye at (x, t) (in moles); C_∞ is the concentration of dye in the pipette; and $\Phi(t)$ is an empirically determined, dimensionless "temporal forcing function," which represents the normalized time course with which dye concentration in the cell at the pipette position equilibrates with the dye in the pipette (see Eq. A9).

Temporal forcing function

The dimensionless temporal forcing function is defined as follows:

$$\Phi(t) = \int_0^t f_{\tau_1} * f_{\tau_2} * f_{\tau_3}\, dt', \tag{A9}$$

where $f_{\tau_i} = (1/\tau_i) \cdot \exp(-t'/\tau_i)$, and * signifies convolution. It might be thought that the dye in the cell at the pipette position would equilibrate to C_∞, the pipette concentration, either instantaneously or along a first-order exponential trajectory. Empirically, however, the fluorescence in the outer segment at the pipette position rose to the equilibrated value along a more complicated, though monotonic, course (see Figs. 8, 10, and 11). This slowed rise in fluorescence probably reflects a limitation on the flux of the dye through the pipette constriction (Pusch and Neher, 1988), a limitation which varies from cell to cell due to the nature of the patching process. Rather than attempt to make an explicit physical model of the dye movement through the pipette constriction, we chose an empirical approach, embodied in the forcing function, $\Phi(t)$.

Solution

The diffusion equation (Eq. 2), subject to the initial and boundary conditions described above, was solved by the method of separation of variables, using Duhamel's theorem for the time-dependent boundary condition at the pipette position (Özişik, 1980; Carslaw and Jaeger, 1959). The

solution, in terms of x^- and x^+, is as follows:

$$C(x^-, t) = \frac{2C_\infty D_x}{p} \sum_{n=0}^{\infty} \alpha_n \cos(\alpha_n x^-) \times \int_0^t \Phi(t)\exp[-(\alpha_n^2 D_x + v_L)(t - \tau)]\, d\tau \quad \text{(A10)}$$

$$C(x^+, t) = \frac{2C_\infty D_x}{l - p} \sum_{m=0}^{\infty} \beta_m \sin(\beta_m x^+) \times \int_0^t \Phi(t)\exp[-(\beta_m^2 D_x + v_L)(t - \tau)]d\tau. \quad \text{(A11)}$$

Here

$$\alpha_n = \frac{-1^{(n+1)}(2n + 1)\pi}{2p} \quad \text{and} \quad \beta_m = \frac{(2m + 1)\pi}{2(l - p)} \quad \text{(A12)}$$

are the eigenvalues for the two compartments. The convolution integrals in Eqs. A10 and A11 were solved with the Laplace transform method, yielding a readily computable, analytic expression for each set of parameters.

A profile of the dye concentration, $C(x,t)$ for $0 \leq x \leq l$, $t \geq 0$ was then obtained by applying the transformations of Eqs. A1 and A2.

No-flux boundary condition

It may seem strange that our formulation allows for a loss of dye along the length of the cell (Eq. 2), yet it stipulates that there is no flux of dye at the two ends of the cell (Eqs. A5 and A6). We did this not because we believe that the end membranes are fundamentally different, but because allowing a flux across the ends (i.e., a radiation boundary condition) resulted in a series solution which did not converge. However, the error resulting from the approach taken should be slight. Taking 25 μm as the average length and 5 μm as the average radius, and treating the rod outer segment as uniform cylinder, the ratio of the surface area of the sides to the surface area of the ends is 5:1. Thus, the sides of the outer segment would be expected to account for five times more flux of dye than the ends. In fact, the rod outer segment is not a smooth cylinder, there being numerous shallow infoldings of the plasma membrane (see, e.g., Fig. 5 and 6), which would tend to increase the relative proportion of "side" membrane. Thus, the no-flux boundary condition at the ends of the cell should not be an unreasonable approximation.

Parameter ranges

The longitudinal diffusion model incorporates six adjustable parameters: χ, τ_1, τ_2, τ_3, S, v_L. Following are brief descriptions of the rationale for the numerical ranges over which each parameter was allowed to vary in attempting to fit the data.

Tortuosity, viscosity, binding: χ

The parameter χ is a dimensionless factor that combines the potential effects of tortuosity, cytoplasmic viscosity, and binding of the diffusing substance to relatively immobile sites (see Eq. 4). In mathematical terms,

$$\chi \equiv \frac{F_A}{\eta F_V B}, \quad \text{(A13)}$$

where F_A/F_V is a measure of tortuosity, i.e., the physical hindrance to longitudinal diffusion arising from the disc stack (Lamb et al., 1981), and η is the ratio of cytoplasmic viscosity to that of water.

Tortuosity can be quantified by the ratio of the patent cross-sectional area to the patent volume available for longitudinal diffusion (F_A/F_V) (Lamb et al., 1981). To see why this is so, consider the random walk of a dye molecule in the outer segment. Imagine that the molecule has an equal probability of stepping in any direction, and is reflected by any solid boundary (i.e., plasma membrane or disc membrane) which it encounters. The probability that the molecule will undergo a net longitudinal displacement is directly proportional to the patent cross-sectional area (F_A): the greater the proportion of the cross-section that is *not* occupied by the discs (i.e., the greater F_A), the greater the probability that the molecule will *not* be relected back by a collision with the disc surface, but instead will find a path through to the next interdiscal space. A similar consideration applies to the patent volume (F_V), but here the relationship is inversely proportional. With a greater proportion of the outer segment volume occupied by the discs, there is, necessarily, less volume occupied by the space between the discs. Therefore, the molecule will spend relatively less time in the inter-discal space, and relatively more time crossing the disc barrier. From measurements of electron micrographs of salamander rod outer segments, we estimated a value of 0.028 for F_A/F_V (see Results).

Although we have not measured η, the viscosity of outer segment cytoplasm, experiments with several cell types (including skeletal muscle fibers, erythrocytes, and a fibroblast cell line) using various methods have produced estimates of cytoplasmic viscosity between 1.3 and 5 times that of water (Kushmerick and Podolsky, 1969; Mastro et al., 1984; Luby-Phelps et al., 1986; Fushimi and Verkman, 1991).

Binding of dye to disc-associated or soluble proteins can be expected to produce two distinct effects on the measured fluorescence. First, dye binding will lower the effective diffusion coefficient, which will manifest itself as a lowered rate of spread of fluorescence. Second, dye binding can be expected to increase the total dye concentration at equilibrium; this in turn will increase the fluorescence intensity over that which would have been observed in the absence of binding. Increased dye concentration due to binding also introduces the potential for self-screening.

We adopted a relatively simple scheme for binding of the dye. Our model assumes that there are a large number

of low-affinity sites that equilibrate rapidly to changes in dye concentration. Thus, the effective diffusion coefficient will be inversely proportional to the buffering ratio, B, defined above (cf. Eq. 4). At first glance it seems that the effects of dye binding might not be empirically distinguishable (with our measurements) from the effects of tortuosity and viscosity. However, as we show later, as the system approaches equilibrium at long times after whole-cell access, dye binding produces a pattern of fluorescence behavior quite distinct from that produced by simply lowering D_x. We chose the range $1 \leq B \leq 10$ for the buffering ratio parameter B.

Combining the values given above for tortuosity, viscosity and binding yields the range: $0.00056 \leq \chi \leq 0.014$.

Temporal forcing function parameters: τ_1–τ_3

The shape of the temporal forcing function, $\Phi(t)$ (which ranges from 0 to 1), is determined by the time constants τ_1–τ_3. The ranges used for the three time constants were 0.2 ms $\leq \tau_1 \leq$ 100 s and 2.0 ms $\leq \tau_2, \tau_3 \leq$ 500 s.These ranges were empirically determined to provide sufficient flexibility to fit the time course to reach equilibration for all of the cells. No a priori constraints were placed on the time constants in determining these ranges.

Loss rate constant: v_L

In case the rate of loss varied significantly from cell to cell, the loss rate constant, v_L, was allowed to vary over the range ($0 \leq v_L \leq 0.1\ s^{-1}$). The actual range needed to fit the fluorescence profiles for the CF cells was $0 \leq v_L \leq 0.02\ s^{-1}$. For the fl-cGMP cells, the theoretical profiles providing the best fit to the data were obtained with $v_L = 0$.

Scaling factor: S

The scaling factor, S, took into account the composite effect of several factors on the overall fluorescence intensity: the collection efficiency of the microscope objective, the sensitivity and efficiency of the image intensifier and CCD camera, and the gain settings of the A-to-D converter in the image processor. The magnitude of this parameter is determined by the fluorescence intensity at long times after whole-cell access, when the cell has reached equilibration with the pipette. The range of S for fitting all 16 cells was $216 \leq S \leq 5780$ p.a. per quanta$\cdot\mu m^{-2}\cdot s^{-1}$ fluorescence emission (empirically determined).

REFERENCES

Baylor, D. A., T. D. Lamb, and K. W. Yau. 1979. Responses of retinal rods to single photons. *J. Physiol. (Lond.).* 288:613–634.

Baylor, D. A., B. J. Nunn, and J. L. Schnapf. 1984. The photocurrent, noise and spectral sensitivity of rods of the monkey, *Macaca fascicularis*. *J. Physiol. (Lond.).* 357:575–607.

Blaurock, A. E., and M. H. F. Wilkins. 1969. Structure of frog photoreceptor membranes. *Nature (Lond.).* 233:906–909.

Cameron, D. A., and E. N. Pugh, Jr. 1990. The magnitude, time course and spatial distribution of current induced in salamander rods by cyclic guanine nucleotides. *J. Physiol. (Lond.).* 430:419–439.

Caretta, A., A. Cavaggioni, and R. T. Sorbi. 1985. Binding stoichiometry of a fluorescent cGMP analogue to membranes of retinal rod outer segments. *Eur. J. Biochem.* 153:49–53.

Carslaw, H. S., and J. C. Jaeger. 1959. Conduction of Heat in Solids 2nd ed. Oxford University Press, Oxford.

Cote, R. H., and M. A. Brunnock. 1993. Intracellular cGMP concentration in rod photoreceptors is regulated by binding to high and moderate affinity cGMP binding sites. *J. Biol. Chem.* In press.

Fushimi, K., and A. S. Verkman. 1991. Low viscosity in the aqueous domain of cell cytoplasm measured by picosecond polarization microfluorimetry. *J. Cell Biol.* 112:719–725.

Gras, W. J., and C. R. Worthington. 1969. X-ray analysis of retinal photoreceptors. *Proc. Natl. Acad. Sci. USA.* 63:233–238.

Hagins, W. A., R. D. Penn, and S. Yoshikami. 1970. Dark current and photocurrent in retinal rods. *Biophys. J.* 10:380–412.

Kawamura, S., and M. Murakami. 1989. Regulation of cGMP levels by guanylate cyclase in truncated frog rod outer segments. *J. Gen. Physiol.* 94:649–668.

Konishi, M., A. Olson, S. Hollingworth, and S. M. Baylor. 1988. Myoplasmic binding of Fura-2 investigated by steady-state fluorescence and absorbance measurements. *Biophys. J.* 54:1089–1104.

Kushmerick, M. J., and R. J. Podolsky. 1969. Ionic mobility in muscle cells. *Science (Wash., DC),* 166:1297–1298.

Lamb, T. D., P. A. McNaughton, and K. W. Yau. 1981. Spatial spread of activation and background desensitization in toad rod outer segments. *J. Physiol. (Lond.).* 319:463–496.

Lamb, T. D., and E. N. Pugh, Jr. 1992. A quantitative account of the activation steps in phototransduction in amphibian photoreceptors. *J. Physiol. (Lond.).* 449:719–758.

Longsworth, L. G. 1953. Diffusion measurements, at 25°, of aqueous solutions of amino acids, peptides and sugars. *J. Am. Chem. Soc.* 75:5705–5709.

Luby-Phelps, K., F. Lanni, and D. L. Taylor. 1986. Probing the structure of cytoplasm. *J. Cell Biol.* 102:2015–2022.

Mastro, A. M., M. A. Babich, W. D. Taylor, and A. D. Keith. 1984. Diffusion of a small molecule in the cytoplasm of mammalian cells. *Proc. Natl. Acad. Sci. USA.* 81:3414–3418.

Mathies, R. A., and L. Stryer. 1986. Single-molecule fluorescence detection: a feasibility study using phycoerythrin. In Applications of fluorescence in the biomedical sciences. D. L. Taylor, A. S. Waggoner, F. Lanni, and R. Birge, editors. Alan R. Liss, Inc., New York. 129–140.

McNaughton, P. A., L. Cervetto, and B. J. Nunn. 1986. Measurement of the intracellular free calcium concentration in salamander rods. *Nature (Lond.).* 322:261–263.

Nakatani, K., and K.-W. Yau. 1988. Guanosine 3′,5′-cyclic monophosphate-activated conductance studied in a truncated rod outer segment of the toad. *J. Physiol. (Lond.).* 395:731–753.

Özişik, M. N. 1980. Heat Conduction. John Wiley & Sons, New York.

Perri, M. 1991. Spatial distribution and kinetics of the light-sensitive current in isolated photoreceptor outer segments dialyzed with cGMP or GTP. Ph.D. thesis, University of Pennsylvania, University Microfilms International, Ann Arbor, MI.

Pugh, E. N., Jr., and T. D. Lamb. 1990. Cyclic GMP and calcium: the internal messengers of excitation and adaptation in vertebrate photoreceptors. *Vision Res.* 30(12):1923–1948.

Pugh, E. N., Jr., and T. D. Lamb. 1993. Amplification and kinetics of the activation steps in phototransduction. *Biochim. Biophys. Acta.* 1141:111–149.

Pusch, M., and E. Neher. 1988. Rates of diffusional exchange between small cells and a measuring patch pipette. Pflügers Arch. *Eur. J. Physiol.* 411: 204–211.

Rink, T. J., R. Y. Tsien, and T. Pozzan. 1982. Cytoplasmic pH and free Mg^{2+} in lymphocytes. *J. Cell Biol.* 95:189–196.

Rosenkranz, J. 1977. New aspects of the ultrastructure of frog rod outer segments. *Int. Rev. Cytol.* 50:25–158.

Sather, W. A., and P. B. Detwiler. 1987. Intracellular biochemical manipulation of phototransduction in detached rod outer segments. *Proc. Natl. Acad. Sci. USA.* 84:9290–9294.

Stryer, L. 1986. Cyclic GMP cascade of vision. *Annu. Rev. Neurosci.* 9:87–119.

Torre, V., H. R. Matthews, and T. D. Lamb. 1986. Role of calcium in regulating the cyclic GMP cascade of phototransduction in retinal rods. *Proc. Natl. Acad. Sci. USA.* 83:7109–7113.

Yau, K.-W., and K. Nakatani. 1985. Light-suppressible cyclic GMP-sensitive conductance in the plasma membrane of a truncated rod outer segment. *Nature (Lond.).* 317:252–255.

Announcement

Issues of the *Biophysical Journal* from volume 1 to the end of 1991 are available. The cost of packing and freight is to be paid by the receiver. Contact: Dr. C. E. Challice, Department of Physics and Astronomy, University of Calgary, Calgary, Alberta Canada, T2N 1N4 Canada. Tel.: 403-220-6059; Fax: 403-289-3331.